Satellite Inference of Thermals and Cloud-Base Updraft Speeds Based on Retrieved Surface and Cloud-Base Temperatures

YOUTONG ZHENG

Department of Atmospheric and Oceanic Science, and Earth System Science Interdisciplinary Center, University of Maryland, College Park, College Park, Maryland, and Institute of Earth Sciences, Hebrew University of Jerusalem, Jerusalem, Israel

DANIEL ROSENFELD

Institute of Earth Sciences, Hebrew University of Jerusalem, Jerusalem, Israel

ZHANQING LI

Department of Atmospheric and Oceanic Science, and Earth System Science Interdisciplinary Center, University of Maryland, College Park, College Park, Maryland, and State Laboratory of Earth Surface Processes and Resource Ecology, and College of Global Change and Earth System Science, Beijing Normal University, Beijing, China

(Manuscript received 30 September 2014, in final form 16 February 2015)

ABSTRACT

Updraft speeds of thermals have always been difficult to measure, despite the significant role they play in transporting pollutants and in cloud formation and precipitation. In this study, updraft speeds in buoyancy-driven planetary boundary layers (PBLs) measured by Doppler lidar are found to be correlated with properties of the PBL and surface over the Southern Great Plains (SGP) site operated by the U.S. Department of Energy's Atmospheric Radiation Measurement Program (ARM). Based on the relationships found here, two approaches are proposed to estimate both maximum (W_{max}) and cloud-base (W_{cb}) updraft speeds using satellite data together with some ancillary meteorological data of PBL depth, wind speed at 10-m height, and air temperature at 2-m height. The required satellite input data are cloud-base and surface skin temperatures. PBL depth can be determined by using cloud-base temperature in combination with European Centre for Medium-Range Weather Forecasts (ECMWF) interim reanalysis data. Validation against lidar-measured updraft speeds demonstrated the feasibility of retrieving W_{max} and W_{cb} using high-resolution *Suomi–National Polar-Orbiting Partnership* Visible Infrared Imaging Radiometer Suite (*Suomi-NPP* VIIRS) measurements over land for PBLs with thermally driven convective clouds during the satellite overpass time. The root-mean-square errors (RMSE) of W_{max} and W_{cb} are 0.32 and 0.42 m s^{-1}, respectively. This method does not work for a stable or a mechanically driven PBL.

1. Introduction

Thermals (buoyancy-driven updrafts within the cloud-free boundary layer) transfer and distribute heat, moisture, momentum, and pollutant materials from the surface layer to the upper part of the convective mixed layer. In addition, they play a central role in the formation of convective clouds and precipitation. Cloud-base updrafts govern water vapor supersaturation, affecting the activation of cloud condensation nuclei (CCN) and thus cloud droplet number concentration (Twomey 1959; Ghan et al. 1993; Reutter et al. 2009). Such microphysical effects of cloud-base updrafts on clouds modulate aerosol impacts on cloud properties, posing a challenge for disentangling aerosol from updraft impacts on cloud microstructure. Hence, updraft velocity retrieval is critical to advancing our understanding of aerosol cloud-mediated effects.

Corresponding author address: Zhanqing Li, Department of Atmospheric and Oceanic Science, and Earth System Science Interdisciplinary Center, University of Maryland, College Park, 5825 University Research Court, Suite 4001, College Park, MD 20740-3823.
E-mail: zli@atmos.umd.edu

DOI: 10.1175/JAS-D-14-0283.1

© 2015 American Meteorological Society

Currently, updraft speeds are estimated in two ways: in situ measurements by towers and aircraft (Lenschow and Stephens 1980; Greenhut and Singh Khalsa 1982; Saïd et al. 2010) and remote sensing by vertically pointing radars and lidars (Kollias et al. 2001; Ansmann et al. 2010). The former methods suffer from the shortcoming of limited spatial coverage, and the latter method is limited by sparse radar or lidar coverage, especially in the vertical dimension. Because of the absence of well-established methods for satellite remote sensing of updrafts, together with the scarcity of the aforementioned traditional updraft velocity measurements, there are very few observations of updraft speeds. Unlike other cloud physics variables (e.g., effective radius of cloud droplets, cloud optical depth, and liquid water path), cloud-base updraft velocity has never been retrieved from satellites. This gap has hampered progress in understanding aerosol–cloud interactions and their effects on climate, as envisioned by the Clouds, Hazards, and Aerosols Survey for Earth Researchers (CHASER) satellite mission (Rosenfeld et al. 2012; Rennó et al. 2013). CHASER is based on the notion of using the base of convective clouds as CCN chambers to retrieve activated CCN at convective cloud base. Rosenfeld et al. (2014a) used combined satellite and radar measurements with satisfactory accuracy (the fractional estimation error is 13%) to estimate the number concentrations and supersaturation of activated CCN at convective cloud base and pointed out that a satellite estimate of convective base updraft, which is required to demonstrate the concept of CHASER, is yet to be developed. This motivated us to develop a method for estimating convective cloud-base updraft from satellites. Updraft retrieval for the nonconvective, mechanically driven PBL is beyond the scope of the current study.

In a convective PBL, buoyancy is the dominant mechanism driving turbulence and, hence, thermals (Young 1988a,b). This dominant role of buoyancy was quantitatively reflected by convective velocity scale w_* introduced by Deardorff (1970), which is written as

$$w_* = \left[\frac{g z_i}{T_v}\overline{(w'T_v')}_s\right]^{1/3}, \tag{1}$$

where g is the acceleration of gravity, z_i is the PBL height, T_v is the mixed-layer mean virtual temperature, and $\overline{(w'T_v')}_s$ stands for the vertical kinetic heat flux near the surface. The convective velocity scale has been demonstrated to effectively scale turbulence velocities in experimental studies (Kaimal et al. 1976; Druilhet et al. 1983), and other studies have used this scale to estimate the quantitative structure of updrafts of the convective PBL by observation (Manton 1977; Lenschow and Stephens 1980; Greenhut and Singh Khalsa 1982, 1987; Chandra et al. 2010) and modeling (Schmidt and Schumann 1989).

Thus, the convective velocity scale constitutes an alternative means of estimating vertical velocity using z_i and $\overline{(w'T_v')}_s$ in the convective PBL. However, great uncertainties in surface heat flux estimation represent a serious barrier to a useful estimation of convective velocities. This study addresses this practical problem by approximating the effects of surface heat flux using the ground–air temperature difference and surface wind as proxies for surface heat fluxes.

Since the satellite inference of updraft speeds is the focus of this study, priority will be given herein to those introduced input parameters that can be derived from satellite measurements.

The following section introduces the theoretical basis for updraft speed retrieval. Section 3 describes the datasets used in this study and the data processing methods. Major findings are presented in section 4. Section 5 summarizes the result of this work and presents its potential applications.

2. Theoretical basis

According to the traditional model first proposed by Taylor (1916), $\overline{(w'T_v')}_s$ is proportional to the wind speed multiplied by the temperature difference between the ground and the air, which could be expressed by a bulk aerodynamic formula:

$$\overline{(w'T_v')}_s = C_H V(T_s - T_a), \tag{2}$$

where C_H is the bulk transfer coefficient, V is the mean surface wind speed, and T_s and T_a are surface skin temperature and air temperature at a reference level (typically 2 m AGL), respectively. According to Eq. (2), fluxes approach zero in the limit of calm winds, which is unlikely to happen in the real atmosphere. In the convective PBL, the well-mixed layer is usually capped by an inversion layer. When thermals approach the inversion base, they will gradually lose their buoyancy as a result of downward heat flux, spread out laterally, and then fall back into the mixed layer as downdrafts, forming convective circulation (Fig. 1). In this case, even when the horizontal mean vector wind is zero, the horizontal mean scalar wind should be nonzero because of the near-surface random perturbation gusts caused by convective circulation (Deardorff 1972; Schumann 1988).

The vector velocity of the horizontal gust speed in the surface layer is usually assumed to be of order w_* (Businger 1973; Schumann 1988). This modifies Eq. (2) in the following way:

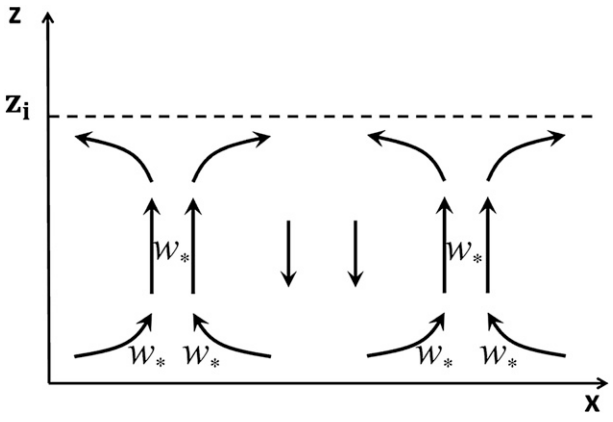

FIG. 1. Schematic of idealized convective circulation [adapted from Stull (1985)]. The updraft velocity and surface-layer gusts have a magnitude of w_*, according to the Deardorff convective scale.

$$\overline{(w'T_v')_s} = C_H(V + w_*)(T_s - T_a), \tag{3}$$

which is similar to an expression proposed by Stull (1994).

Under the condition of free convection, where the turbulent energy is generated by buoyancy forces and where the mean horizontal wind vanishes, Eq. (3) reduces to

$$\overline{(w'T_v')_s} = C_H w_*(T_s - T_a). \tag{4}$$

Substituting Eq. (4) into Eq. (1), we have

$$w_* = \left[\frac{gz_i}{T_v} C_H(T_s - T_a)\right]^{1/2}. \tag{5}$$

Equation (5) shows that the scale of convective velocity is proportional to the square root of the product of PBL height and the ground–air temperature difference in the regime of extreme free convection.

3. Data and methodology

The research area in this paper centers on the Atmospheric Radiation Measurement Program (ARM) Southern Great Plains (SGP) Central Facility (CF) site (36.6°N, 97.5°W) located to the southeast of Lamont, Oklahoma. The land cover consists of cattle pasture and crop fields (detailed information about the CF site can be found at http://www.arm.gov/sites/sgp). We utilize both ground-based ARM datasets and space-borne measurements from the Visible Infrared Imaging Radiometer Suite (VIIRS) onboard the *Suomi–National Polar-Orbiting Partnership* (*Suomi-NPP*) satellite, as well as ERA-Interim data. The *Suomi-NPP* overpasses the SGP site twice daily. We used the *Suomi-NPP* measurements in the afternoon near 1330 local solar time, when the convective PBL is well formed, singling out the dominant role of thermals. Based on VIIRS imagery over the SGP site, a total of 84 clear-PBL cases and 28 cloud-topped-PBL cases were selected from July 2012 to November 2013 based on the following objective criteria:

- Thermally driven boundary layer clouds were selected. Therefore, cases with clouds that are decoupled from the boundary layer were excluded. A cloud is regarded as being coupled with the surface fluxes if the cloud-base height measured by ceilometer or lidar agreed with the lifting condensation level (LCL) to within 200 m. The LCL was calculated based on surface temperature and dewpoint. The vertical continuity of thermals from surface to cloud base during these conditions was verified by the Doppler lidar velocity and reflectance features extending from near surface to cloud base.
- Only single-layer boundary layer clouds are considered. Cases with multilayer low clouds or with mid- or high-level clouds that obscure the surface and PBL clouds were excluded. Cases with semitransparent high-level clouds were also excluded, because they distort the radiative signals from the surface and PBL clouds. Such clouds were identified according to the 11–12-μm brightness temperature difference and by elevated 1.3-μm reflectance as measured by the *Suomi-NPP* VIIRS.
- The determination of cloud-base temperature is based on the algorithm developed by Zhu et al. (2014), who utilized the visible reflectance and a homogeneity parameter of 11.45-μm brightness temperature from the *Suomi-NPP* VIIRS imager to determine cloud-base temperature. Note that this method is not valid for all clouds but convective ones of certain size. The algorithm fails for very small clouds (smaller than 750 m horizontally), which cannot fill the pixel (750 m × 750 m) of the *Suomi-NPP* VIIRS.
- Downdrafts due to precipitation can obscure the signal as a result of thermals. Therefore, precipitating clouds were excluded. We identified rain as reflectivity streaks extending from within the clouds to surface according to time–height images of radar reflectivity.

a. Data

1) GROUND-BASED DATA

The ground-based observations in this paper were made at the ARM SGP CF site and the collaborating extended facility (EF) site. Specific data are as follows:

(i) The 10-m horizontal wind speed and 2-m air temperature data are obtained from the ARM Surface Meteorology System (MET). The 1-min statistics of air temperature at 2 m and arithmetic-averaged and vector-averaged wind speed and direction at 10 m are obtained. We took 1-h averages of these quantities centered on the *Suomi-NPP* overpass time.

(ii) Vertical profiles of the horizontal wind speed and temperature are provided by a balloon-borne sounding system (SONDE). Balloons are launched four times per day at the SGP site. We selected the one at approximately 1130 LT that is about 2 h before satellite overpasses.

(iii) PBL height is obtained from the PBL height value-added product (VAP). This VAP implements three different methods for estimating PBL heights from radiosonde data. In this study, we use the one based on methods developed by Heffter (1980). For the five cases without PBL height observations, we roughly estimate PBL heights by selecting the height at which Doppler lidar signals decrease abruptly. While this was done subjectively, the height is very clear for convective PBLs, and measurements done by different people are not likely to yield very different results.

(iv) Cloud-base height is measured by the Vaisala ceilometer (VCEIL).

(v) Vertical velocity data is from the Doppler lidar. The method of calculating the updraft speeds using Doppler lidar will be described in section 3b.

2) SATELLITE-BASED DATA

Suomi-NPP, launched on 28 October 2011, carries an imaging instrument, VIIRS. This instrument provides spatial resolution of up to 375 m for wave bands that allow the retrieval of cloud temperature and microphysical properties. This resolution is a vast improvement over the 1000 m of the Moderate Resolution Imaging Spectroradiometer (MODIS). Rosenfeld et al. (2014b) demonstrate the unique capabilities of high-resolution *Suomi-NPP* VIIRS to retrieve cloud properties. Zhu et al. (2014) utilize the *Suomi-NPP* VIIRS imager to retrieve cloud-base temperature with a standard error of only 1.1°C. All the satellite datasets over the SGP site in this study are provided by *Suomi-NPP* VIIRS:

(i) Cloud-top temperature T_{ct} is calculated using Rosenfeld et al.'s (2014b) method of utilizing the brightness temperature difference between the band of 10.8 and 12.0 μm for cloud-top temperature retrieval.

(ii) Cloud-base temperature T_{cb} is retrieved using the method developed by Zhu et al. (2014). The method is based on finding the warmest cloudy pixels from a running window of *Suomi-NPP* VIIRS.

(iii) Surface skin temperature is provided by VIIRS land surface temperature (LST) environmental data record (EDR) at a spatial resolution of about 0.75 km at nadir and about 1.3 km at the edge of the swath. The LST EDR products are averaged within a 0.25° × 0.25° area. Considering the advection of thermals by horizontal winds, we calculate the 1-h vector mean of 10-m wind direction and select the 0.25° × 0.25° region for averaging upwind from the SGP site. Using data quality flags, we discard samples that are contaminated by thin cirrus. In cloudy cases, although the satellite cannot retrieve the surface temperature under clouds, convective clouds always leave holes between them with valid LST data. These data points are averaged in the 0.25° × 0.25° area. The reason we use spatial average of satellite-retrieved T_s instead of surface measurements of T_s is that T_s depends highly on surface type, and any single point measurements of T_s cannot represent the large-scale surface forcing that drives the updrafts.

3) REANALYSIS DATA

The datasets from the ECMWF interim reanalysis are utilized. These include 2-m air temperature, 10-m wind speed, surface geopotential, and vertical profiles of geopotential and wind speeds. The temporal resolution is 6 h, and the spatial resolution is 1.25° × 1.25°. Temporal and spatial interpolations are used to spatiotemporally match Doppler lidar and satellite data used in this study.

b. *Updraft speed calculation with Doppler lidar measurements*

The validity of Doppler lidar retrieval of PBL parameters has been demonstrated in multiple studies (Tucker et al. 2009; Ghate et al. 2014). In 2010, three new coherent Doppler lidar systems were acquired by the ARM Climate Research Facility. One of them was deployed at the SGP. Doppler lidar was used to measure the vertical velocity of aerosol particles from 15 m AGL to the top of the PBL with approximately 1-s temporal and 30-m vertical resolution. The transmitted wavelength is 1.5 μm.

There are several advantages to using coherent Doppler lidar to retrieve vertical velocity. First, Doppler lidar uses aerosol particles as atmospheric scattering targets. Aerosol particles are excellent tracers of air

motions. In contrast to radar, lidar is capable of measuring wind velocities under clear-sky conditions with very good precision (better than 0.1 m s^{-1}). Second, taking advantage of the Doppler frequency shift, Doppler lidar provides a large Nyquist interval of 19 m s^{-1} for vertical velocity, which is 3 times larger than that for radar at the SGP site. Third, lidar-retrieved velocity is much less sensitive to bias by falling rain drops than is radar-retrieved vertical air velocity.

Retrieval uncertainty in updraft speed is mainly a result of the turbulent nature of updrafts. Turbulent updrafts are typically characterized by a wide distribution of vertical velocities. The quantification of these vertical velocities into one value of updraft speed depends on what we use the updraft speed for. Here, we would like the updraft speeds to be weighted by the created cloud volume by the updrafts at cloud base. Therefore, we determine the effective updraft speed using the formula

$$W = \left.\frac{\sum N_i W_i^2}{\sum N_i W_i}\right|_{W_i > W_{\text{thre}}}, \tag{6}$$

where N_i stands for the frequency of occurrence of vertical velocity W_i on the histogram of vertical velocity distribution. A threshold value of vertical velocity W_{thre} is required to define the updrafts (Lenschow and Stephens 1980). We'll discuss how to determine W_{thre} in the next section.

Equation (6) is capable of weighing the cloud volume created by cloud-base updrafts because of the following. For a given W_i, the horizontal area that it covers at a certain height can be characterized by the frequency of its occurrence N_i. Therefore, it is reasonable to view $N_i W_i$ at cloud base as the cloud volume created by W_i. Replacing $N_i W_i$ in Eq. (6) with the cloud volume created by W_i (Volume$_i$) leads to

$$W = \left.\frac{\sum \text{Volume}_i W_i}{\sum \text{Volume}_i}\right|_{W_i > W_{\text{thre}}}, \tag{7}$$

which is actually the volume-weighted mean of the vertical velocity distribution. Equation (7) represents the potential influence of all the vertical velocities larger than W_{thre} on the creation of cloud volume and justifies using Eq. (6) for quantifying the spectrum of updraft speeds into one number.

1) DETERMINING W_{thre}

To find an appropriate representation of updrafts, we examine different percentiles of vertical velocity as the threshold values for the definition of updrafts (Fig. 2). Three representative cases (24 March, 25 June, and 2 February 2013) are presented. The vertical red lines in the left panels mark the *Suomi-NPP* satellite overpass time in order to temporally match the land surface temperature retrieved by VIIRS. As denoted by the boxes in the height–time displays of lidar vertical velocity data (Figs. 2a,c,e), 1-h Doppler lidar pixels of vertical velocity within 200-m layers were used to calculate the updraft velocity using Eq. (6). In cloudy conditions, we selected a 2-h (rather than 1-h) time window that centers on satellite overpass time for cloud-base updraft calculation in order to include more cloudy pixels. Admittedly, the selection of a 1- or 2-h time window is somewhat arbitrary. Sensitivity tests (not shown) suggest that the computed updrafts are not sensitive to the time window if the selected time window captures several convective cells that pass overhead, which corresponds to 1–2 h. If the time window is too short, say 10 min, then it cannot even capture a complete thermal so that the insensitivity will not hold anymore. Another reason to use a long time window (1–2 h) is that a sufficient number of lidar samples can be collected to represent the updrafts on a large scale and therefore spatially match T_s that is averaged over a 0.25° × 0.25° region. A horizontal wind speed of 5–10 m s^{-1} integrates over a spatial scale of several tens of kilometers within 1–2 h. To visualize the PBL top (the top boxes in Figs. 2a,c,e) and rule out noises, pixels with signal-to-noise ratio (SNR)—which is calculated as the ratio of the integrated signal to the noise floor integrated over the passband—less than 0.012 were excluded.

As shown in Fig. 2, the vertical distribution and absolute value of the updraft speeds are not sensitive to the percentile of the vertical velocity that is used to define W_{thre}. Considering the minor difference among the updraft speeds, with W_{thre} defined by varying percentiles of vertical velocity, in the remaining part of this article, we simply select the updraft velocity with $W_{\text{thre}} = 0$.

2) DATA QUALITY CONTROL

In section 3a(1), we use the SNR of 0.012 as a threshold value to remove noisy pixels. Data quality is nonetheless not ensured, since in specific cases noisy pixels may still contain important information, even if the SNR is set to 0.012. We tested the sensitivity of the updraft velocity to SNR threshold and found that the retrieved updrafts are highly independent of the threshold for SNR at height levels within the PBL top for 85% cases (not shown). However, this insensitivity diminishes when PBLs are very deep (>2.5 km). Indeed, the insensitivity is not present in 9 out of 84 clear cases and 8 out of 28 cloudy cases. In the upper part of the deep PBL, lidar returns are sometimes very weak

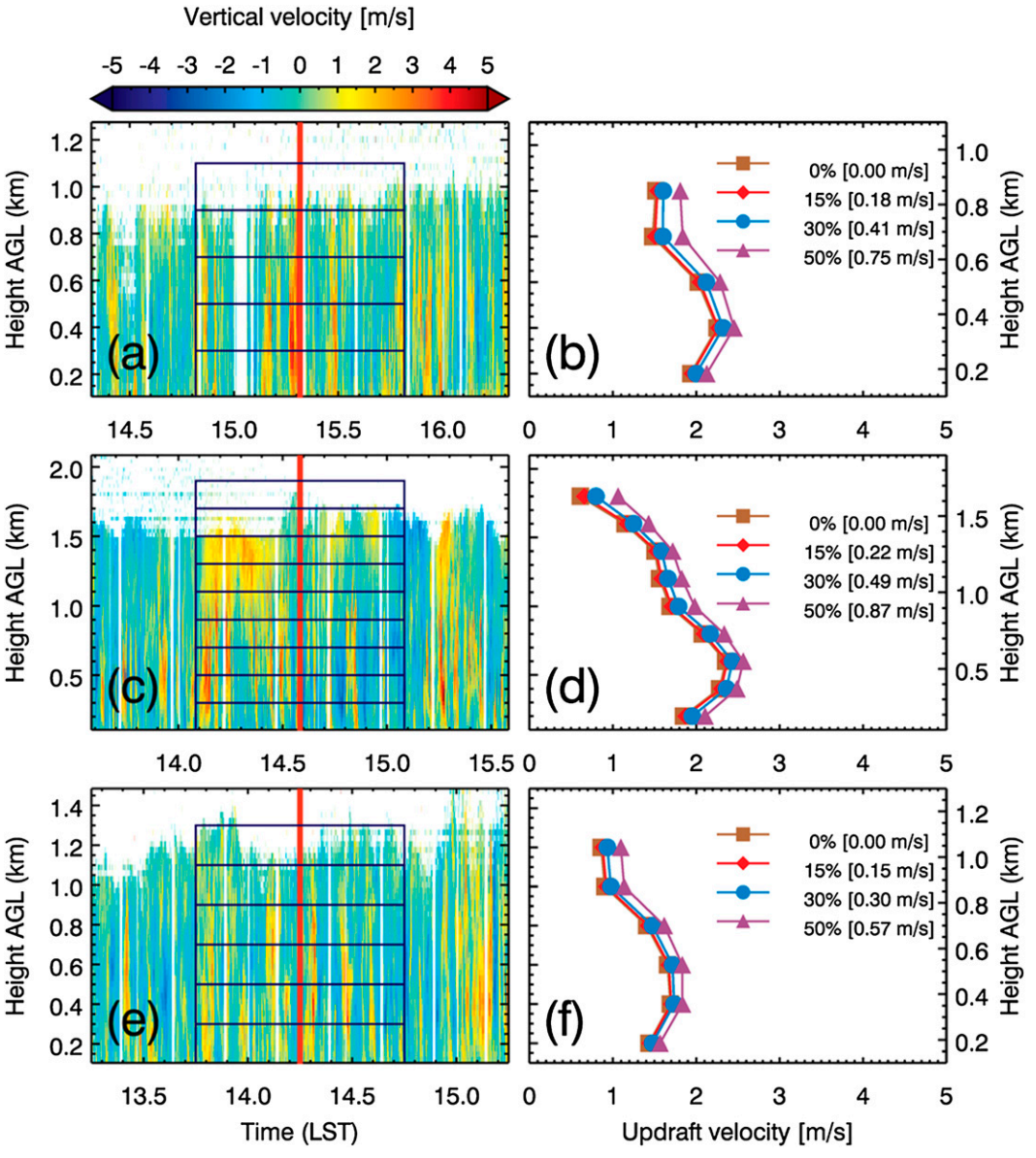

FIG. 2. Three representative cases on (a),(b) 24 Mar; (c),(d) 25 Jun; and (e),(f) 2 Feb 2013. (a),(c),(e) Height–time display of vertical-staring data from Doppler lidar in SGP site. SNR is set to 0.012 to visualize the PBL tops. Red lines mark the *Suomi-NPP* overpass times. Black rectangles denote the height–time areas within which vertical velocity pixels are selected for updraft speed calculation using Eq. (6). (b),(d),(f) Corresponding calculated updraft speeds at each height for different percentiles of vertical velocity (0%, 15%, 30%, and 50%). The values in the brackets denote the corresponding threshold vertical velocity used to define updraft.

because returning signals are mostly attenuated because of the long distance between lidar and aerosol particles. In this situation, lidar updraft signals are usually indistinguishable from noises; too many useful pixels are removed with increasing SNR threshold. This is illustrated in Figs. 3a and 3b, which show the height–time image of Doppler lidar for the case on 13 July 2012. The convective cloud-base height in this case is about 2740 m AGL, as detected by VCEIL. Each box encloses an area with 200-m height and 2-h width centered on the *Suomi-NPP* overpass time marked by the red vertical lines. The top box corresponds to cloud base. Figure 3a, with an SNR threshold of 0.005, shows the clear structure of vertical velocities in the PBL. Many randomly distributed pixels in the free atmosphere, however, suggest the existence of a certain amount of noise. When we increase the SNR threshold to 0.013 (Fig. 3b), most noisy pixels are filtered out.

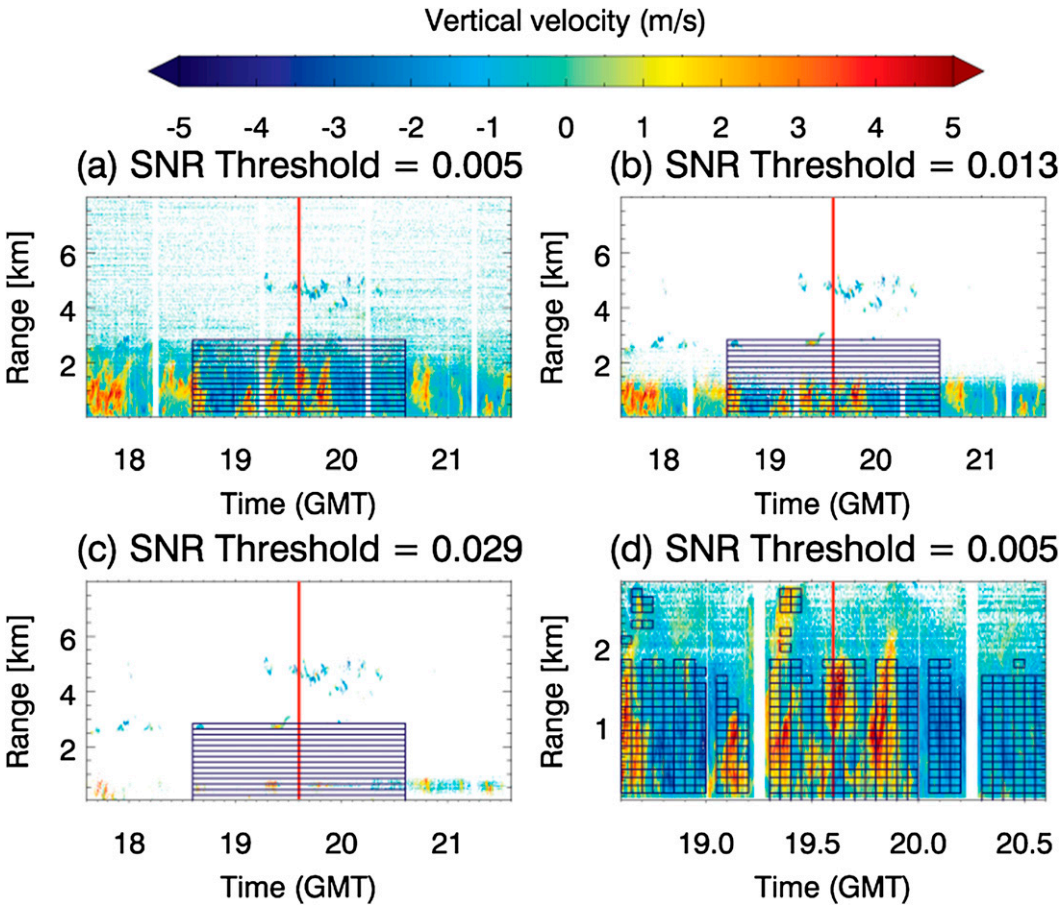

FIG. 3. Height–time display of vertical-staring data from the Doppler lidar at the SGP site on 13 Jul 2012 with SNR threshold of (a) 0.005, (b) 0.013, and (c) 0.029. Black rectangles with 2-h time window and 200-m height window denote the areas within which vertical velocity pixels are selected for updraft speed calculation using Eq. (6). (d) As in (a), but with shorter height range (up to a PBL top of 2740 m) and shorter time range (2 h). Boxes in (d) stand for continuous unit areas. Red lines mark the *Suomi-NPP* overpass time for all four panels.

However, the signals in the higher part of the PBL are also lost with the increasing SNR threshold.

To solve this problem for deep PBL cases, we developed a new technique that filters out noise with relatively minor signal loss. The technique is based on the assumption that the distribution of atmospheric variables is locally continuous. This assumption is supported by Fig. 3a, showing that the lidar pixels within updrafts or downdrafts are continuous, whereas pixels outside thermals are comparatively discontinuous, especially in the upper part of the PBL, which has weak lidar returns. Thus, signal pixels can be distinguished from noise pixels by identifying the continuity of their distribution. Based on this principle, we selected lidar pixels according to the following procedure:

(i) In the height–time display of Doppler lidar, divide the area of interest into many smaller unit areas with 100-m height and 3-min width. Each unit area contains about 450 pixels.

(ii) Increase the SNR threshold to a value that filters out noisy pixels but does not mar the clear structure of the PBL in the lidar image (0.005 for the case in Fig. 3). Although the determination of this SNR threshold value needs visual judgment, the calculated updraft speeds based on this algorithm are not sensitive to the SNR threshold selected in this step. The main impact of losing the signal is loss of the updraft speed altogether from the higher parts of the PBL.

(iii) Define as "continuous" those unit areas with a ratio larger than 90% of the number of remaining pixels after thresholding to the total number of pixels within the unit area (~450 pixels) (continuous unit areas for the example case are plotted in Fig. 3d).

(iv) All the pixels within continuous unit areas are used to calculate updraft speeds. For pixels outside continuous unit areas, only those pixels with an

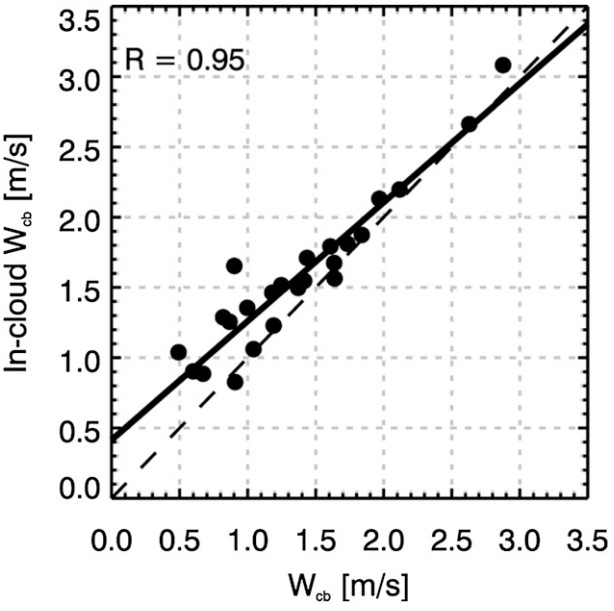

FIG. 4. Comparison between in-cloud W_{cb} and W_{cb} calculated using the input of vertical velocities selected according to our new technique. One data point represents a cloudy case. Solid and dashed lines are linear fit and one-to-one line, respectively. The correlation coefficient is given.

SNR larger than the threshold that filters most noises (0.013 for the case in Fig. 3) are selected.

To test the validity of this technique, we assume that cloud-base updraft is continuous through cloud base, which means that cloud-base updraft speed in cloud should be consistent with the updraft speed just below the cloud base (Kollias et al. 2001). If our technique is valid, cloud-base updraft speed W_{cb} calculated using Eq. (6) with inputs from our technique should be in agreement with the in-cloud W_{cb} that can be obtained by selecting cloudy pixels at cloud base by increasing the SNR threshold so that only cloudy pixels remain. Comparison of these two cloud-base updraft speeds shows good agreement (Fig. 4) with correlation coefficient $R = 0.95$. This confirms the validity of the technique herein proposed. In addition, we also find that in-cloud W_{cb} is slightly larger than W_{cb}, owing to the enhanced buoyancy induced by latent heat release during the condensation process. Such acceleration behavior is more significant for cases with weak updrafts. Assuming the near square root dependence of kinetic energy on vertical velocity, the same increase in kinetic energy leads to a larger relative increase in vertical velocity for small vertical velocity.

In the remaining sections, we simply select the maximum updraft speed W_{max} in the vertical. We do this for two reasons. First, W_{max}, least affected by entrainment, reflects best the impacts of surface heat flux. Second, although PBL depth varies among different cases because of differing degrees of surface heating, W_{max} generally occurs at $z/z_i = 0.3$ in clear-sky conditions (Lenschow and Stephens 1980; Chandra et al. 2010), where z_i is the PBL depth. In this case, the advantage of using W_{max}, but not at an arbitrary height, is its generalization potential to all conditions of varying degrees of surface heating and PBL depth during different seasons.

4. Results

a. Clear boundary layer

1) Updraft estimation based on wind variation

As shown in section 3, if a convective circulation is formed, the horizontal gusts caused by convective circulation are on the magnitude of the convective velocity scale. We assume that the horizontal wind can be separated into slowly varying large-scale mean wind and rapidly varying local circulation-induced wind components. In this case, the variability of winds, characterized by standard deviation of wind speed, should be mainly attributed to the gusts caused by the convective circulation (Deardorff 1972), which is shown in Fig. 1.

The above-noted reasoning connects updrafts with surface wind variability, as demonstrated in Fig. 5a. Each point in Fig. 5a represents one case that corresponds to a single satellite overpass time over the SGP site. For each case, the time window of lidar is 1 h so that it contains several thermal events. The standard deviation of winds and updraft speeds are calculated at the 30-min time range, which is about the time scale of convective circulation. Figure 5a shows a nonlinear increase of W_{max} with surface wind variation. Since there is no theoretical basis for the quantification of this relationship, we assume a linear relationship for simplicity. A correlation coefficient of 0.63 between W_{max} and wind variation was found. The statistically significant level p according to a t test is less than 0.001, indicating a 99.9% confidence level. Data were partitioned into three equal-sized subsets differentiated by horizontal mean wind speed, as shown in the figure legend, and each subset contains 27 cases. The results show a positive correlation between W_{max} and surface wind variation for light wind ($V < 4.3\,\mathrm{m\,s^{-1}}$) and moderate wind ($4.3 < V < 6.7\,\mathrm{m\,s^{-1}}$) conditions. This relation deteriorates when the surface winds are strong ($V > 6.7\,\mathrm{m\,s^{-1}}$). This is reflected by the decreased correlation coefficient (R goes from 0.69 and 0.71 to 0.37). The underlying physical process is that, for strong winds, mechanical eddies caused by strong wind shear rip apart the developing thermals and thereby strongly perturb the convective circulation (Stull 1994).

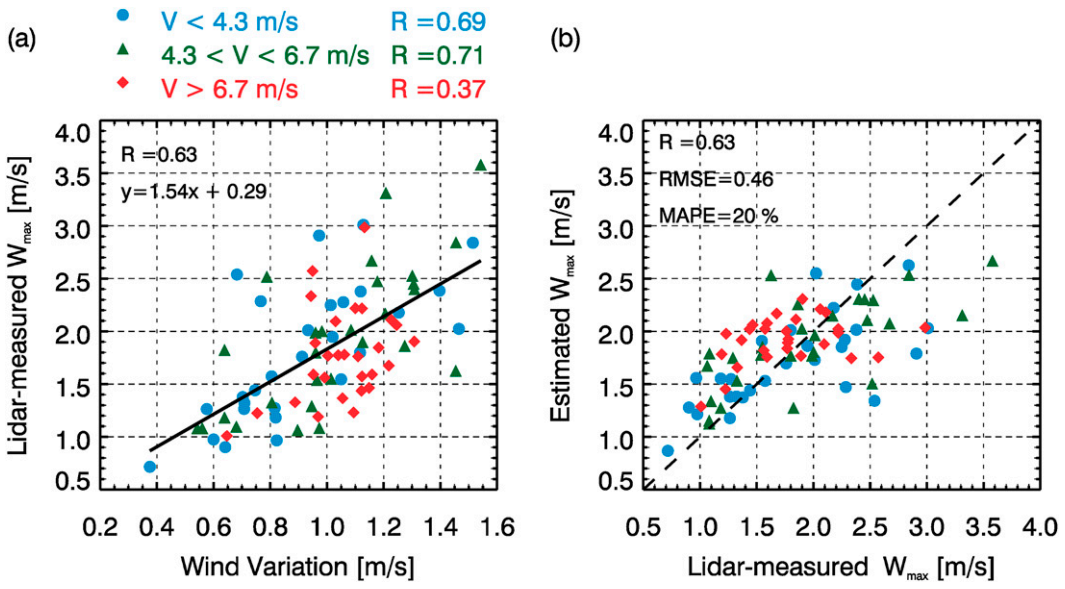

FIG. 5. (a) Variation of lidar-measured W_{max} with surface horizontal wind variation (standard deviation of wind speeds) in the clear PBL. The value of R and the linear-fit line are given with respect to the full datasets. (b) Comparison between estimated W_{max} by wind variation using the relation shown in (a) and lidar-measured W_{max}. The values of R, RMSE, and MAPE are given. The correlation is significant at the 99.9% confidence level based on a t test. The correlation coefficients for each subset in (b) are identical to those in (a).

To test the ability of the relation found here to predict updraft speed, we estimate W_{max} using the observed wind variation (WV) and the best-fit linear regression equation:

$$W_{est} = A_1 \mathrm{WV} + A_2, \tag{8}$$

where A_1 and A_2 are the coefficients of the regression equation ($A_1 = 1.54$ and $A_2 = 0.29$, as shown in Fig. 5a). Comparison of the estimated W_{max} and the lidar-measured W_{max} is present in Fig. 5b. The root-mean-square error (RMSE) and mean absolute percentage error (MAPE) are $0.46\,\mathrm{m\,s^{-1}}$ and 20%, respectively. Unlike vertical velocity, surface wind is more widely observed. In areas where surface wind observations with sufficient time resolution are available, we can utilize Eq. (8) to estimate the updraft speeds with a standard error of about $0.46\,\mathrm{m\,s^{-1}}$.

2) UPDRAFTS ESTIMATION BASED ON SURFACE AND PBL PROPERTIES

Recalling Eq. (5) in section 3, the convective velocity scale should be linearly proportional to the square root of the product of z_i and the ground–air temperature difference $(T_s - T_a)$. Based on this theoretical relation, we assume

$$W_{est} = B_1 [z_i (T_s - T_a)]^{1/2} + B_2, \tag{9}$$

where B_1 and B_2 are coefficients that could be assumed as constants here, although they may be functions of other factors affecting updraft speeds, such as air drag, surface wind speed, and PBL wind shear. We determine the value of B_1 and B_2 by taking the linear regression analysis between lidar-measured W_{max} and observed $[z_i(T_s - T_a)]^{1/2}$. With the value of the coefficients ($B_1 = 0.24$ and $B_2 = 0.99$) and observed $[z_i(T_s - T_a)]^{1/2}$, we calculate W_{max} and validate it by lidar-observed W_{max} (Fig. 6a). The correlation coefficient is 0.74, and the RMSE is $0.34\,\mathrm{m\,s^{-1}}$. When the surface wind speed is large ($V > 6.7\,\mathrm{m\,s^{-1}}$), on the one hand, the correlation coefficient decreases because of the decreasing robustness of the free convection assumption. On the other hand, updraft speeds for strong wind cases tend to be underestimated, which is consistent with the idea that enhanced shear-driven eddies facilitate the transport of heat in the surface layer, increasing buoyancy and, hence, updraft speed.

Hence, taking into account surface wind speed as well as ground–air temperature difference and PBL height results in a more universal estimation of updraft speed. Given the complex and possibly chaotic impacts of mechanical turbulence on thermals, the incorporation of surface wind speed into Eq. (9) in a way that has a physical basis seems a daunting task. Here, we only consider the facilitating effect of mean wind on the vertical transport of heat in the surface layer. In Eq. (9), which is based on the free convection assumption, $T_s - T_a$ characterizes the transport of heat caused by temperature gradient. Assuming that wind-induced

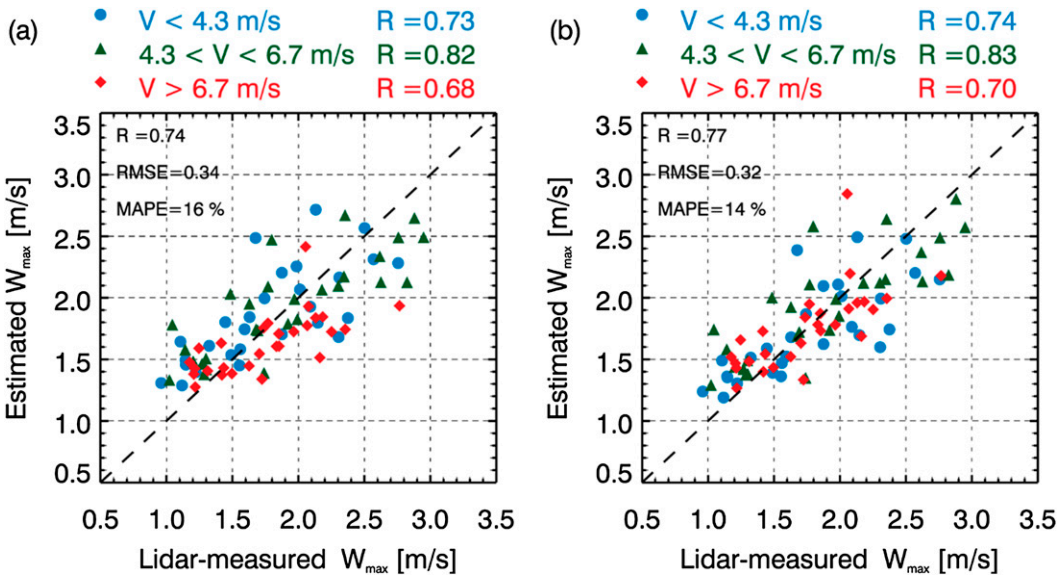

FIG. 6. Comparisons between lidar-measured W_{max} and (a) estimated W_{max} based on Eq. (9) without the surface wind and (b) estimated W_{max} based on Eq. (10), which corrects for the surface wind. The values of R, RMSE, and MAPE are given for the full datasets in each panel. Both correlations are significant at the 99.9% confidence level based on a t test.

transport of heat, characterized by $V(T_s - T_a)$ based on Taylor's equation (Taylor 1916), is quasi independent of transport action resulting from $T_s - T_a$, we perform a linear superposition of these two terms, yielding

$$W_{est} = C_1[z_i(1 + C_M V)(T_s - T_a)]^{1/2} + C_2, \quad (10)$$

where C_1 and C_2 are coefficients. The mechanical transport coefficient for heat C_M is found empirically to be 0.25 (Fig. 6b) by taking the linear regression between W_{max} and $[z_i(1 + C_M V)(T_s - T_a)]^{1/2}$ with the use of different values of C_M and selecting the value corresponding to the largest R. Apart from physical considerations, another reason we include wind speed in our method in the form of Eq. (10) is that it accounts for situations wherein surface mean wind ceases. In fact, in calm wind conditions where wind speed approaches zero, Eq. (10) reduces to Eq. (9), and our method still works with a valid theoretical basis. The value of W_{max} estimated by Eq. (10) is in statistically better agreement with lidar-measured W_{max} than that by Eq. (9) according to the larger R, smaller RMSE, and smaller MAPE (Fig. 6b). In addition, points with different wind speeds distribute more uniformly in Fig. 6b than in Fig. 6a, further confirming the universality of using Eq. (10) to estimate updraft speeds.

After demonstrating the effects of shear-induced eddies on enhancing the heat flux in the surface layer, it is informative to see if mechanical eddies play a role in the well-mixed layer. Here we use the wind shear (WS), calculated by dividing the horizontal wind speed difference between PBL top and surface by PBL depth, to characterize the mixed-layer mechanical eddies. Then, we examined the variation of ratio of estimated W_{max} by Eq. (10) to measured W_{max} with wind shear and found no correlation (not shown). This indicates that for clear PBL the accuracy of our method of estimating W_{max} is not affected by PBL wind shear. Actually, the wind shear and surface wind speed V are not independent. Much of the wind shear effect may already be accounted for by V in Eq. (10).

b. *Cloud-topped boundary layer*

1) RETRIEVAL OF W_{max}

Cloud behavior is regarded as an important factor in the modification of subcloud-layer (well-mixed layer) dynamic systems (Stull 1985; Neggers et al. 2006). However, because of the complicated processes and feedbacks in this coupled system of cloud and subcloud layers, a well-established theoretical framework quantifying the impacts of cloud behavior on subcloud-layer updrafts is still missing. Does our algorithm of estimating W_{max} also apply to cloud-topped PBL? The answer is yes, as shown in Fig. 7. Figures 7a and 7b show W_{max} estimated based on Eqs. (8) and (10), respectively, validated by lidar-measured W_{max} in cloudy condition (black lines and dots). Here, we take the 1-h (instead of 30 min for clear-PBL cases) standard deviation of surface wind speed to represent the wind variation because

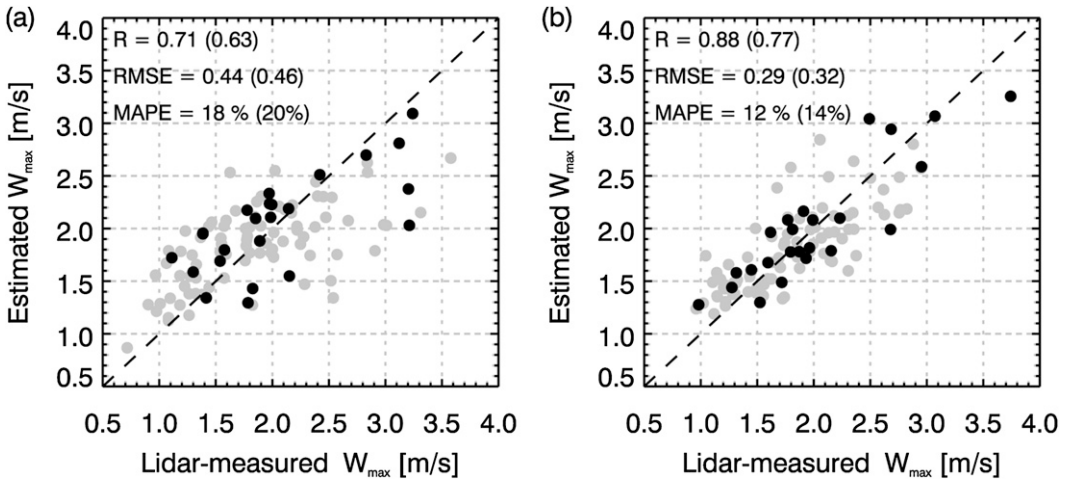

FIG. 7. Comparisons between lidar-measured $W_{\max}$ and (a) estimated $W_{\max}$ based on wind variations [Eq. (8)] and (b) estimated $W_{\max}$ based on V, T_s, T_a, and z_i [Eq. (10)] for cloudy (black) and clear (gray) PBL cases. Because Doppler lidar observations are not available for 4 of the 28 cloudy cases, only 24 cases were plotted. The values of R, RMSE, and MAPE are given for the datasets corresponding to black points and gray points in each panel. Values in the parentheses correspond to gray points. Both correlations are significant at the 99.9% confidence level.

the time scale of convective circulation is usually longer in a cloudy PBL as a result of deeper circulation. We also use the cloud-base height $H_{\rm cb}$ to replace z_i in Eq. (10) since $H_{\rm cb}$ is easier to retrieve from a satellite with satisfactory accuracy [this will be demonstrated in section 4b(3)]. Here it should be emphasized that the assumed equality of PBL height and $H_{\rm cb}$ may not always be valid. Nonetheless, according to the theory introduced in section 2, the PBL top is identified with the height that thermals can reach. The processes pertaining to wet thermals, driven partially by latent heating in cloud, are beyond the scope of the theory considered in this study. Therefore, when clouds are present, the cloud-base height, which is at the top of the dry thermals, is a valid approximation of PBL height, at least for this specific study.

Comparison of estimated updraft speeds in cloudy (black lines and dots) and clear PBL (gray lines and dots) suggests that in cloud-topped PBL we can estimate $W_{\max}$ with relatively better agreement with lidar-measured $W_{\max}$ in view of R, RMSE, and MAPE. This is consistent with the idea that convective circulation is more likely to be well formed when convective clouds are present. Generally, thermals produced from surface heating may die before reaching the PBL top. This is caused mainly by the entrainment of environmental air into the rising thermals. When clouds are present, there must be thermals with sufficient intensity to reach cloud base to trigger them in the first place.

Figure 8a shows that, unlike in clear-sky conditions, cloud-topped-PBL wind shear appears to affect updraft speeds. With the enhancement of wind shear, the ratio of updraft speed estimated by Eq. (10) to lidar-measured updraft speed decreases. A negative correlation coefficient of -0.42 was found, which is statistically significant at the 95% confidence level based on a t test. In other words, we tend to overestimate $W_{\max}$ when the wind shear is strong. A possible explanation may be that the shear-induced eddies can rip thermals apart, thus weakening updraft speeds. The more well-formed convective circulation under cloudy conditions amplifies the signal of wind shear's impact on thermals that cannot be detected in clear-sky conditions. In addition, the deeper PBL (1.59 km on average for cases in this study) for cloudy conditions than for clear conditions (1.19 km on average) provides more room for shear-induced mechanical eddies to impinge on the thermals.

To take advantage of the above-noted finding, we simply multiply the right-hand side of Eq. (10) by the regression equation between wind shear and the ratio of updraft speed estimated by Eq. (10) to lidar-measured updraft speed, to yield the following equation:

$$W_{\rm est} = (D_1 \mathrm{WS} + D_2)\{C_1[z_i(1 + C_M V)(T_s - T_a)]^{1/2} + C_2\}, \quad (11)$$

where D_1 and D_2 are coefficients for wind shear correction. For $W_{\max}$ estimation in cloudy PBL, $D_1 = -0.02$ and $D_2 = 1.08$, as shown in Fig. 8a. Figure 8b shows the slightly improved estimation of $W_{\max}$ by Eq. (11) (black lines and dots) compared with that estimated by Eq. (10) (gray lines and dots) in terms of R, RMSE, and MAPE.

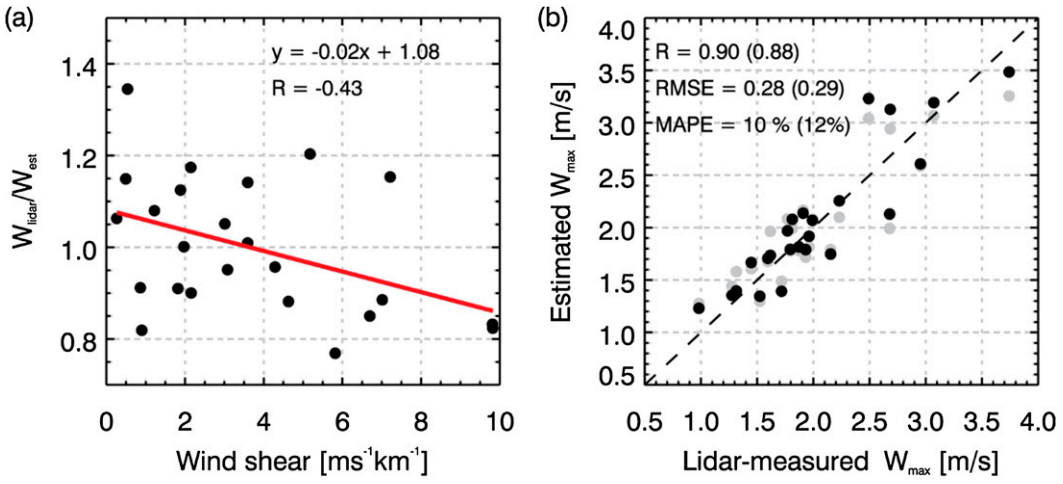

FIG. 8. (a) Variation of ratio of lidar-measured W_{max} to estimated W_{max} with wind shear for cloud-topped-PBL conditions. The value of R and the best-fit line are given. The correlation is significant at the 95% confidence level. (b) Comparison between lidar-measured W_{max} and estimated W_{max} based on Eq. (11), which applies a wind shear correction (black), and Eq. (10), which does not correct for wind shear (gray). The values of R, RMSE, and MAPE are given for the datasets corresponding to black points and gray points in each panel. Values in the parentheses correspond to gray points. The correlation is significant at the 99.9% confidence level.

2) RETRIEVAL OF W_{cb}

Compared to W_{max}, W_{cb} is of greater interest because of its significant impact on the formation and evolution of convective clouds (see the introduction). Figure 9 shows a statistically significant correlation ($R = 0.80$) of W_{cb} with W_{max} in cloud-topped PBL. The value of W_{cb} is smaller than W_{max}, which is primarily attributable to a stabilizing of the environment near the top of the mixed layer, though dilution with environmental air and drag may also play a role. We use the temperature difference between satellite-retrieved cloud base and cloud top ($T_{cb} - T_{ct}$) to identify cloud thickness. All 24 cloudy cases here are divided into three equal-sized subsets differentiated by $T_{cb} - T_{ct}$, and each subset contains 8 cases. Based on the limited number of cases, we roughly classify the clouds of the three subsets as thin ($T_{cb} - T_{ct} \le 3°C$), medium-thick ($3° < T_{cb} - T_{ct} \le 11°C$), and thick ($T_{cb} - T_{ct} > 11°C$) clouds. Blue points correspond to thin clouds, and red points represent the medium-thick and thick clouds. Comparison of these two subsets of cases suggests that, on days with thin clouds, W_{cb} tends to be significantly smaller than W_{max}, whereas, for other cases, W_{cb} is comparatively more consistent with W_{max}. This systematic distinction is illustrated in Fig. 10. The thin clouds (left) are usually topped by a strong inversion layer to prevent them from developing. The highly negative buoyancy induced by the strong inversion remarkably decelerates the updraft speeds as they reach cloud base, resulting in a much smaller W_{cb} than W_{max}. In the meantime, the inability to quantify the effects of the entrainment makes it more difficult to estimate W_{cb} after such deceleration, which indicates that, if the satellite-retrieved $T_{cb} - T_{ct}$ is small, the estimated W_{cb} is less reliable. For the clouds with medium or long vertical extent, the updrafts are less influenced by the stabilizing of the entrainment layer. The air rising in the thermals can continue to ascend through the cloud base and circulate through the cloud. In this situation, W_{cb} is more consistent with W_{max}.

Given the statistically significant correlation between W_{max} and W_{cb}, we assume that the approaches of estimating W_{max} introduced in this study are also applicable for W_{cb} estimation. Following the same procedure as estimating W_{max}, we estimated W_{cb} with similar Eqs. (8) and (11), but with different values of the coefficients (Table 1). The calculation of W_{cb} was based on observed wind variation (Fig. 11a) and surface and PBL parameters (Fig. 11b). The correlation coefficients are larger than 0.73, and the RMSEs (MAPEs) are less than 0.42 m s^{-1} (28%) for both W_{cb} estimations validated against those retrieved by Doppler lidar. This demonstrates a useful performance of our method and provides a possibility of estimating W_{cb} based on surface wind variation and on observed surface and PBL parameters (V, H_{cb}, T_s, T_a, and WS). In fact, if we use the calculated W_{max} as an intermediate parameter and the linear regression equation between W_{max} and W_{cb} for estimating W_{cb} (gray points and lines in Figs. 11a and 11b), the results are very similar to the

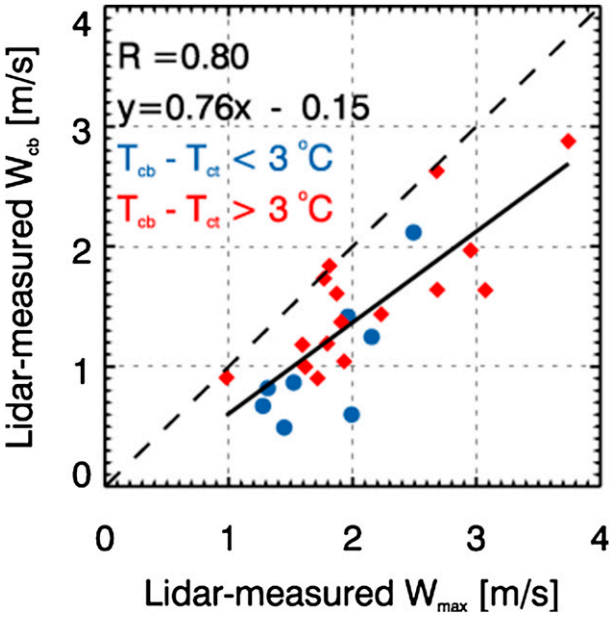

FIG. 9. Comparison between lidar-measured W_{cb} and W_{max}. The value of R and the best-fit line are given for the full datasets. The correlation is significant at the 99.9% confidence level.

direct estimation of W_{cb} (black points and lines). This supports the assumption that the method of estimating W_{max} also works for W_{cb}.

Here, as shown in Table 1, we summarized all the values of the coefficients in Eqs. (8)–(11), which are used to estimate the updraft speeds in clear and cloudy PBLs.

3) FEASIBILITY OF SATELLITE RETRIEVAL OF UPDRAFT SPEEDS

To test the potential for satellite-based application of this relationship, we utilize the ECMWF reanalysis and VIIRS-retrieved data to estimate the inputs for retrieving W_{cb} by the following:

(i) Surface skin temperature can be retrieved by *Suomi-NPP* VIIRS in the same way mentioned in 3a(2).
(ii) The 2-m air temperature and 10-m wind speed can be obtained from the ECMWF reanalysis 2-m air temperature and 10-m wind product, respectively.
(iii) Cloud-base height is retrieved based on VIIRS-retrieved T_{cb} and the air temperature product at 2-m height from the ECMWF reanalysis. We assume that the 2-m air temperature decreases at a dry adiabatic lapse rate until it reaches T_{cb}. The height corresponding to T_{cb} is H_{cb}.
(iv) Wind shear can be obtained with retrieved H_{cb} and vertical profile of wind speed from the ECMWF reanalysis.

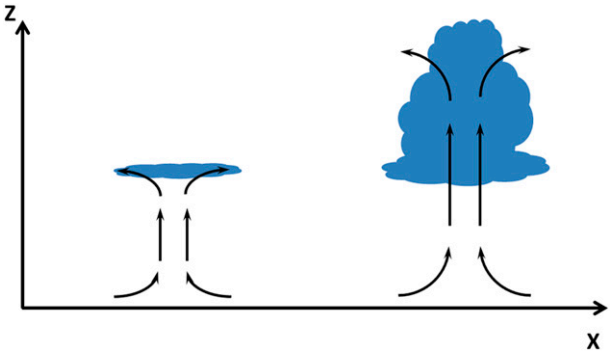

FIG. 10. Schematic diagram showing the difference in convective circulation between (left) thin clouds and (right) clouds with medium and deep extent.

The four parameters derived from satellite and reanalysis data are compared with ARM measurements over the SGP site and shown in Fig. 12. Good agreements were found for H_{cb} and T_a, with correlation coefficients of 0.97 and 0.98, respectively. The RMSE is 1.89°C for T_a and 300 m for H_{cb}, which correspond to MAPE of 4% and 13%, respectively. The good agreement for H_{cb} largely benefits from accurate 2-m air temperature from reanalysis and reliable satellite retrieval of cloud-base temperature (RMSE = 1.1°C). Compared with 2-m air temperature, the estimation of 10-m horizontal wind speed derived by reanalysis is much worse (MAPE = 38%). This can be attributed primarily to the fact that the spatial distribution of horizontal wind speed is much less continuous than that for surface air temperature, in which condition the spatial interpolation will produce larger errors for 10-m wind speed from reanalysis. The quantity least accurately estimated is the wind shear. This is partially caused by high spatial variability of wind speeds measured by instruments onboard the observing platform tethered to the balloon, whereas the vertical profile of ECMWF-based wind speed has already been smoothed. This inconsistency leads to a large discrepancy between SONDE-measured and ECMWF-derived wind shear.

Applying these satellite-retrieved parameters and Eq. (11), we estimate the values for W_{max} and W_{cb} and compare them with those measured by lidar (Fig. 13). RMSEs (MAPEs) are 0.32 m s^{-1} (12%) and 0.42 m s^{-1} (24%) with respect to W_{max} and W_{cb}, respectively. Although the wind shear derived by reanalysis has large errors, it still improves the updraft speed estimation, as shown in Fig. 13. It is interesting to see that the accuracy of satellite-retrieved updrafts is comparable to that retrieved by ground measurements that are expected to be more reliable. The surprisingly good performance of satellite retrieval benefits greatly from

TABLE 1. Summary of coefficients used in updraft estimations.

Equation No.	Estimated parameters (in clear or cloudy PBL)	Coefficient value	Coefficient value
Eq. (8)	W_{max} (clear)	$A_1 = 1.54$	$A_2 = 0.29$
	W_{max} (cloudy)	$A_1 = 2.12$	$A_2 = -0.18$
	W_{cb} (cloudy)	$A_1 = 2.09$	$A_2 = -0.81$
Eq. (9)	W_{max} (clear)	$B_1 = 0.24$	$B_2 = 0.99$
Eq. (10)*	W_{max} (clear)	$C_1 = 0.17$	$C_2 = 0.93$
	W_{max} (cloudy)	$C_1 = 0.27$	$C_2 = -0.18$
	W_{cb} (cloudy)	$C_1 = 0.20$	$C_2 = 0.26$
Eq. (11)**	W_{max} (cloudy)	$D_1 = -0.02$	$D_2 = 1.08$
	W_{cb} (cloudy)	$D_1 = -0.04$	$D_2 = 1.13$

* $C_M = 0.25$ for Eqs. (10) and (11).
** In Eq. (11), the values of C_1 and C_2 are identical to those in Eq. (10) for W_{max} and W_{max} estimation in a cloudy PBL.

the area of coverage of the input variables retrieved by satellite or reanalysis. The satellite-retrieved updrafts are, therefore, on a large scale, which spatially matches the scale of the lidar-measured updrafts. Equation (8) is not tested here for satellite application, because the wind variation, as the only input of Eq. (8), cannot be retrieved by satellite.

The validation results are encouraging. They bolster our confidence in utilizing satellites, augmented by reanalysis data, to estimate updraft speeds in convective PBL with satellite coverage of large areas.

4) LIMITATIONS

The limitations of the method introduced in this study include the following:

(i) The concept of convective velocity scale w_* is based on the Deardorff similarity model that provided, for the past four decades, conceptual foundations for observational and modeling studies on the unstable atmospheric PBL. In recent years, this theory has been questioned in some studies (Smedman et al. 2007; Laubach and McNaughton 2009). McNaughton et al. (2007) pointed out that the observed temperature spectra are not consistent with those predicted by the similarity model. However, the statistically significant correlations (>0.7) found in this study support the theoretical foundation on which they were based. The authors of this study are not aware of a better alternative formulation.

(ii) The theoretical basis of this study assumes convective PBL, and all the cases selected for this study took place in the early afternoon, when turbulence in the PBL is primarily driven by buoyancy. Although we include the effects of wind on facilitating surface heat transport and the impacts of wind shear on weakening updraft speeds, the method is only applicable to the buoyancy-driven PBL, and will fail in the mechanically driven PBL. Its applicability to other phases of the diurnal cycle over land is yet to be determined. The restriction of our method to the buoyancy-driven PBL leads to another practical issue: how do we identify convective PBLs? Typically, convective cloud-topped PBLs are characterized by a dry adiabatic lapse rate below the clouds. Given the satellite-retrieved T_{cb} and vertical profile of temperature from ECMWF reanalysis, we can derive the H_{cb} as the height at which T_{cb} occurs. If this H_{cb} is consistent with the H_{cb} derived by 2-m air temperature from a reanalysis based on the assumption of a dry adiabatic lapse rate, it means that the clouds are coupled with surface heating, indicating a convective PBL. However, this method may depend largely on the reliability of reanalysis-derived vertical profiles of temperature, which requires further study and is not the focus of this paper.

(iii) Because of the difficulty of satellite retrieval of z_i, the method proposed in this study does not permit the satellite retrieval of updraft speeds in the clear PBL. Luo et al. (2014) proposed a method using space-borne lidar to retrieve PBL height with global coverage. Using the PBL height derived by their algorithm or by ECMWF reanalysis, estimating updraft speeds in clear PBL may be possible in the near future.

(iv) The heterogeneities of surface properties can induce mesoscale circulations caused by different turbulent fluxes for different land surfaces (Lynn et al. 1995). Such physical processes are unaccounted for in the theoretical basis of this study, which assumes a homogeneous surface. The satisfying performance of our updraft speed estimation may benefit greatly from the relatively homogeneous landscape over the SGP. For regions without homogeneous surface properties, deviations from our method can occur. Further study is required to examine our method's ability to estimate updraft speeds over regions with varying surface properties.

(v) The method was developed over land surface. Its applicability to sea surface needs to be examined in future studies.

(vi) None of the cases selected for the present study produces precipitation. The boundaries of rain-generated cold pools tend to induce updrafts that are not directly related to the mechanism explored in this study. This will be the subject of future research.

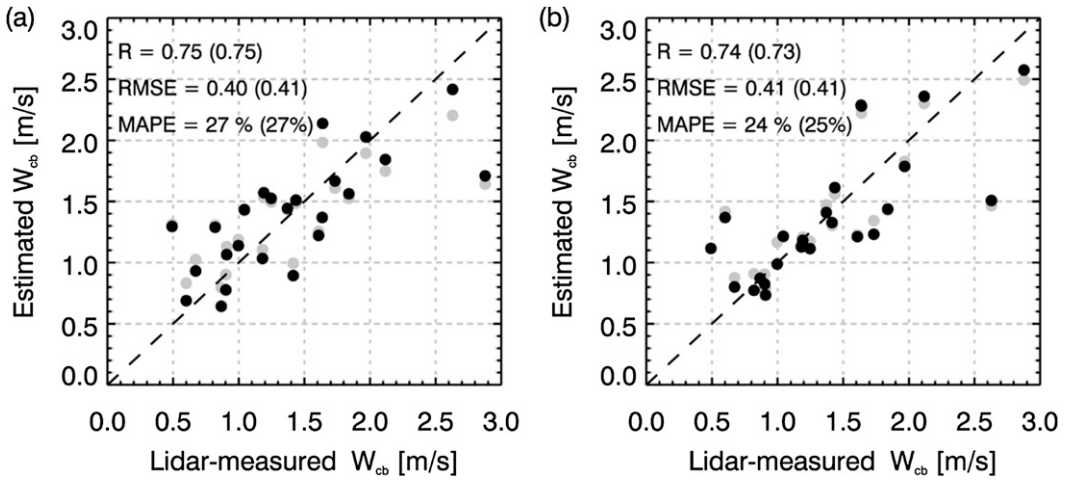

FIG. 11. Validation of estimated W_{cb} based on (a) measured surface wind variations [Eq. (8)] and (b) surface and PBL parameters [Eq. (11)] against lidar-measured W_{cb}. The black and gray points correspond to W_{cb} calculated directly and W_{cb} estimated with the intermediate calculation of W_{max}, respectively. The values of R, RMSE, and MAPE are given for the datasets corresponding to black points and gray points in each panel. Values in the parentheses correspond to gray points. Both correlations are significant at the 99.9% confidence level.

5) IS THE METHOD USEFUL?

The aforementioned limitations of this method are likely to engender doubts regarding its usefulness. Admittedly, the application of our method is limited by two main factors. First, the studied PBL must be buoyantly driven. Second, because of the difficulty of the satellite retrieval of PBL depth, the PBL has to be topped by convective clouds so that we can use satellite-retrieved cloud-base height to approximate PBL depth. Since the retrieval of W_{cb} for convective clouds is of the greatest interest in this study (see the introduction), these two main limiting factors do not affect the major application of the method. As Fig. 13b shows, the MAPE of the satellite-estimated W_{cb}, as validated against lidar data, is 24%. To demonstrate that a MAPE of 24% for W_{cb} is useful for aerosol–cloud interaction studies, we do the following analysis.

Twomey (1959) described the roles of updraft and aerosol number concentration in determining cloud-base supersaturation and droplet concentration with an analytical approximation:

$$N_d = N_{ccn1}^{2/(k+2)} W_{cb}^{3k/(2k+4)}, \tag{12}$$

where N_{ccn1} is the cumulative CCN concentration at 1% supersaturation, W_{cb} is the updraft velocity at cloud base, and k is the slope of CCN supersaturation spectrum in the log–log scale. The values of k in the observed spectra usually lay in the range 0.5–1.0 over continents (Khvorostyanov and Curry 2006), which correspond to an error in N_d (retrieval error and natural variability) of 7%–11%, respectively, when caused by a MAPE of 24% in W_{cb}. This is very useful.

It is noteworthy that the retrieved W_{cb} is not W_{cb} of specific clouds but the integrated W_{cb} for a large area that changes between 300 and 1100 km^2. The values for the range of area we give here are based on the size of the rectangle of the *Suomi-NPP* VIIRS imager that encloses a sufficient number of convective clouds and excludes layer clouds for all the 24 cloudy cases in this study. For cloud–aerosol interaction studies, extensive aircraft measurements have demonstrated robust relations between cloud drop properties and CCN, which are extensive properties of the whole cloud cluster at a time scale of an hour and space scale of several tens of kilometers (Freud et al. 2008; Freud et al. 2011; Freud and Rosenfeld 2012; Rosenfeld et al. 2012). These findings further demonstrate the usefulness of W_{cb} retrieved by the method in this study.

5. Conclusions and potential applications

Based on Doppler lidar, *Suomi-NPP* VIIRS satellite, and conventional in situ measurement data over the Southern Great Plains, we proposed and tested two novel methods of estimating updraft speeds of thermals in the convective PBL. One is based on the correlation between updraft speeds and surface wind variation; the other is based on the effects of surface (V and $T_s - T_a$) and PBL (z_i and wind shear) factors on updraft speeds. These two methods work for both the clear and the cloud-topped convective PBL. Taking advantage of the tight correlation between W_{max} and W_{cb}, we further

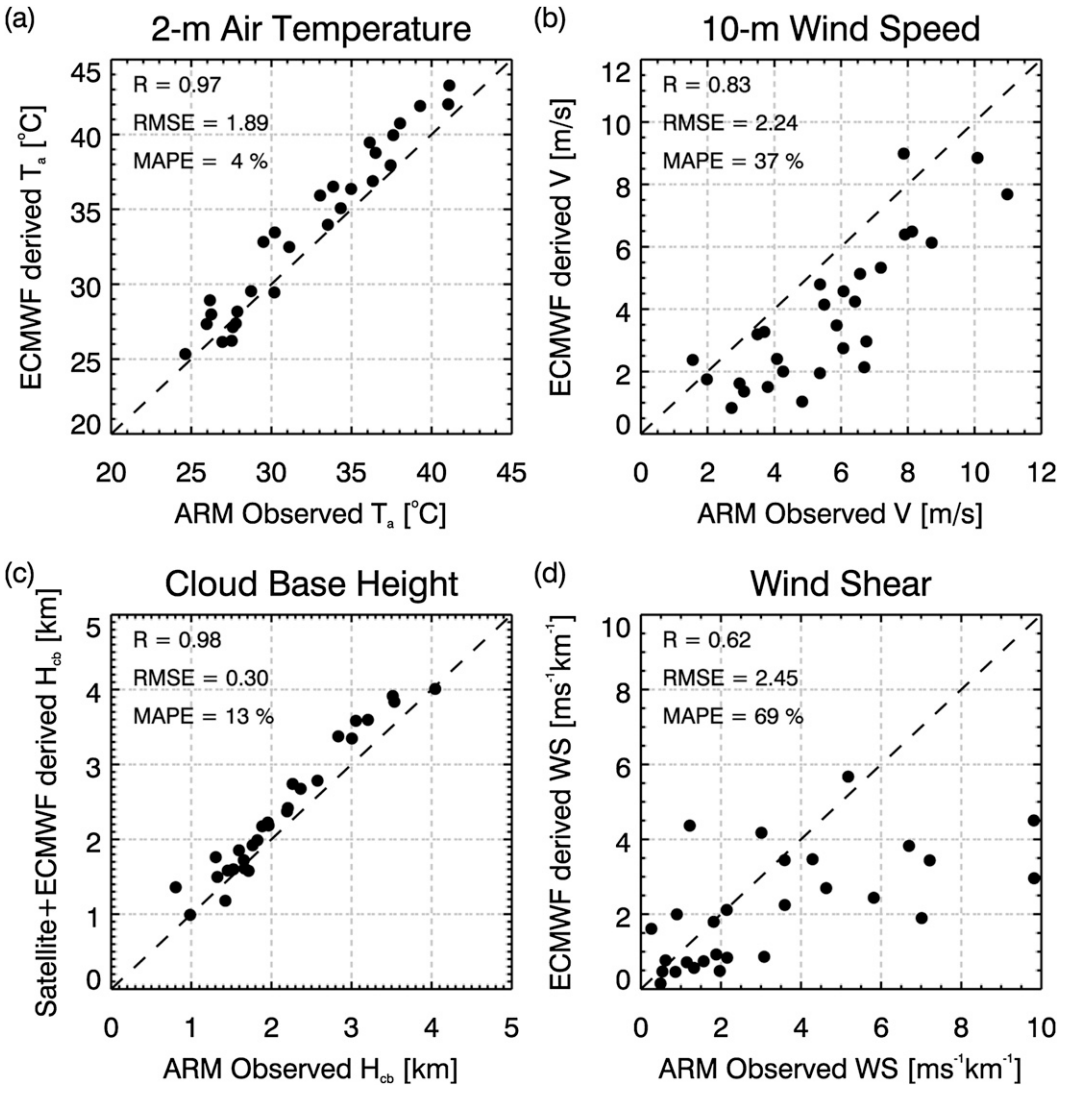

FIG. 12. Comparison between ECMWF- and satellite-derived parameters and those from ARM observation for (a) 2-m temperature, (b) 10-m wind speed, (c) cloud-base height obtained by adiabatic cooling of the surface air temperature to satellite-retrieved cloud-base temperature, and (d) wind shear. The values of R, RMSE, and MAPE are given in each panel.

extend our methods to W_{cb} estimation, showing good agreement with lidar-measured W_{cb}.

To test the feasibility of the satellite retrieval of updraft speeds, we derive the required input parameters (V, H_{cb}, T_s, T_a, and WS) by using *Suomi-NPP* VIIRS in conjunction with ECMWF reanalysis data. From these parameters, we retrieve W_{max} and W_{cb} in the cloud-topped PBL. Comparison of the estimated and lidar-measured updraft speeds shows good agreement (RMSE = 0.32 and 0.42 m s^{-1} with regard to W_{max} and W_{cb}, respectively), demonstrating the feasibility of satellite retrieval of thermals and cloud-base updraft speeds in the cloud-topped PBL. This satellite-based method is not examined in the clear PBL because of the difficulty in retrieving the PBL depth z_i by satellite.

This method contributes to the existing body of knowledge in at least two ways. First, it has not been possible until now to retrieve updraft speed from satellite measurements in buoyancy-driven boundary layers, even though further studies are warranted for operational applications. Second, the method does a good job of retrieving convective W_{cb} by satellite. The 24% of MAPE for W_{cb} retrieval corresponds to an error of 7%–11% in N_d if the CCN supersaturation spectrum is known. This is very useful accuracy for aerosol–cloud interaction studies.

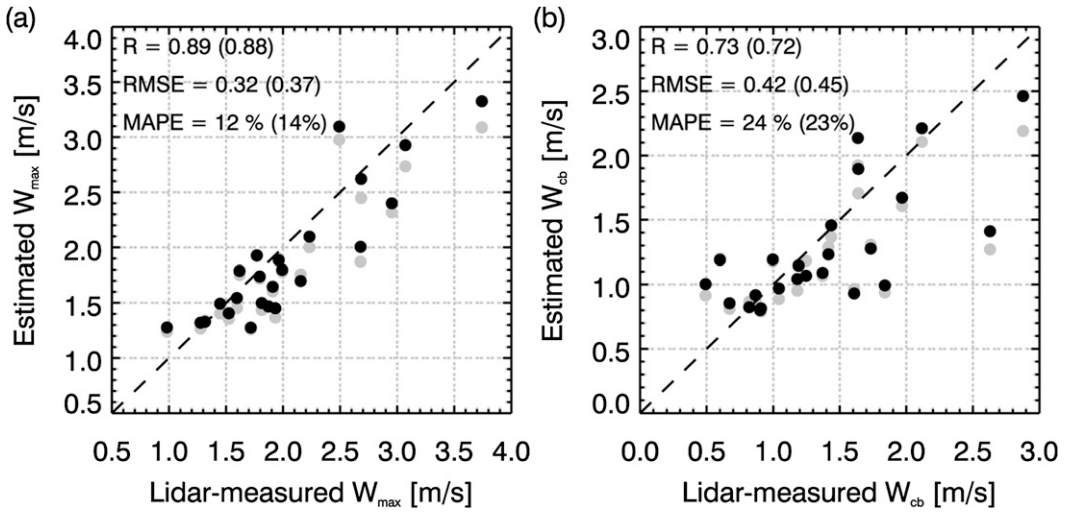

FIG. 13. Validation of satellite-estimated (a) W_{max} and (b) W_{cb} based on Eq. (11), which corrects for wind shear (black), and Eq. (10) without wind shear (gray) against those measured by Doppler lidar. The values of R, RMSE, and MAPE are given for the datasets corresponding to black points and gray points in each panel. Values in the parentheses correspond to gray points. Both correlations are significant at the 99.9% confidence level.

The parameterization of vertical velocity is a core issue in the field of atmospheric numerical modeling. The relationships found in this study significantly deepen our grasp of this pivotal and only partially understood topic.

Acknowledgments. This study was supported by the U.S. Department of Energy (DOE) Office of Science (BER) Atmospheric System Research Program, Grants DE-SC0006787 and DE-SC0007171. The ground-based data in this study are available from the website of the ARM Climate Research Facility (www.archive.arm.gov/data). The satellite-based data can be obtained from the Comprehensive Large Array-Data Stewardship System (CLASS) (www.class.ncdc.noaa.gov/saa/products/search?datatype_family=VIIRS) under the aegis of the National Oceanic and Atmospheric Administration (NOAA). The reanalysis data are available from the website of the ECMWF Data Services (http://apps.ecmwf.int/datasets/data/interim-full-daily/).

REFERENCES

Ansmann, A., J. Fruntke, and R. Engelmann, 2010: Updraft and downdraft characterization with Doppler lidar: Cloud-free versus cumuli-topped mixed layer. *Atmos. Chem. Phys.,* **10,** 7845–7858, doi:10.5194/acp-10-7845-2010.

Businger, J. A., 1973: A note on free convection. *Bound.-Layer Meteor.,* **4,** 323–326, doi:10.1007/BF02265241.

Chandra, A. S., P. Kollias, S. E. Giangrande, and S. A. Klein, 2010: Long-term observations of the convective boundary layer using insect radar returns at the SGP ARM Climate Research Facility. *J. Climate,* **23,** 5699–5714, doi:10.1175/2010JCLI3395.1.

Deardorff, J. W., 1970: Preliminary results from numerical integrations of the unstable planetary boundary layer. *J. Atmos. Sci.,* **27,** 1209–1211, doi:10.1175/1520-0469(1970)027<1209:PRFNIO>2.0.CO;2.

——, 1972: Parameterization of the planetary boundary layer for use in general circulation models. *Mon. Wea. Rev.,* **100,** 93–106, doi:10.1175/1520-0493(1972)100<0093:POTPBL>2.3.CO;2.

Druilhet, A., J. P. Frangi, D. Guedalia, and J. Fontan, 1983: Experimental studies of the turbulence structure parameters of the convective boundary layer. *J. Climate Appl. Meteor.,* **22,** 594–608, doi:10.1175/1520-0450(1983)022<0594:ESOTTS>2.0.CO;2.

Freud, E., and D. Rosenfeld, 2012: Linear relation between convective cloud drop number concentration and depth for rain initiation. *J. Geophys. Res.,* **117,** D02207, doi:10.1029/2011JD016457.

——, ——, M. Andreae, A. Costa, and P. Artaxo, 2008: Robust relations between CCN and the vertical evolution of cloud drop size distribution in deep convective clouds. *Atmos. Chem. Phys.,* **8,** 1661–1675, doi:10.5194/acp-8-1661-2008.

——, ——, and J. Kulkarni, 2011: Resolving both entrainment-mixing and number of activated CCN in deep convective clouds. *Atmos. Chem. Phys.,* **11,** 12 887–12 900, doi:10.5194/acp-11-12887-2011.

Ghan, S. J., C. C. Chung, and J. E. Penner, 1993: A parameterization of cloud droplet nucleation part I: Single aerosol type. *Atmos. Res.,* **30,** 198–221, doi:10.1016/0169-8095(93)90024-I.

Ghate, V. P., B. A. Albrecht, M. A. Miller, A. Brewer, and C. W. Fairall, 2014: Turbulence and radiation in stratocumulus-topped marine boundary layers: A case study from VOCALS-REx. *J. Appl. Meteor. Climatol.,* **53,** 117–135, doi:10.1175/JAMC-D-12-0225.1.

Greenhut, G. K., and S. J. Singh Khalsa, 1982: Updraft and downdraft events in the atmospheric boundary layer over the equatorial Pacific Ocean. *J. Atmos. Sci.,* **39,** 1803–1818, doi:10.1175/1520-0469(1982)039<1803:UADEIT>2.0.CO;2.

——, and ——, 1987: Convective elements in the marine atmospheric boundary layer. Part I: Conditional sampling statistics. *J. Climate Appl. Meteor.,* **26,** 813–822, doi:10.1175/1520-0450(1987)026<0813:CEITMA>2.0.CO;2.

Heffter, J. L., 1980: Transport layer depth calculations. *Bull. Amer. Meteor. Soc.,* **61,** 97–97.

Kaimal, J. C., J. C. Wyngaard, D. A. Haugen, O. R. Coté, Y. Izumi, S. J. Caughey, and C. J. Readings, 1976: Turbulence structure in the convective boundary layer. *J. Atmos. Sci.,* **33,** 2152–2169, doi:10.1175/1520-0469(1976)033<2152:TSITCB>2.0.CO;2.

Khvorostyanov, V. I., and J. A. Curry, 2006: Aerosol size spectra and CCN activity spectra: Reconciling the lognormal, algebraic, and power laws. *J. Geophys. Res.,* **111,** D12202, doi:10.1029/2005JD006532.

Kollias, P., B. A. Albrecht, R. Lhermitte, and A. Savtchenko, 2001: Radar observations of updrafts, downdrafts, and turbulence in fair-weather cumuli. *J. Atmos. Sci.,* **58,** 1750–1766, doi:10.1175/1520-0469(2001)058<1750:ROOUDA>2.0.CO;2.

Laubach, J., and K. McNaughton, 2009: Scaling properties of temperature spectra and heat-flux cospectra in the surface friction layer beneath an unstable outer layer. *Bound.-Layer Meteor.,* **133,** 219–252, doi:10.1007/s10546-009-9422-2.

Lenschow, D. H., and P. L. Stephens, 1980: The role of thermals in the convective boundary layer. *Bound.-Layer Meteor.,* **19,** 509–532, doi:10.1007/BF00122351.

Luo, T., R. Yuan, and Z. Wang, 2014: Lidar-based remote sensing of atmospheric boundary layer height over land and ocean. *Atmos. Meas. Tech.,* **7,** 173–182, doi:10.5194/amt-7-173-2014.

Lynn, B. H., D. Rind, and R. Avissar, 1995: The importance of mesoscale circulations generated by subgrid-scale landscape heterogeneities in general circulation models. *J. Climate,* **8,** 191–205, doi:10.1175/1520-0442(1995)008<0191:TIOMCG>2.0.CO;2.

Manton, M. J., 1977: On the structure of convection. *Bound.-Layer Meteor.,* **12,** 491–503, doi:10.1007/BF00123194.

McNaughton, K. G., R. J. Clement, and J. B. Moncrieff, 2007: Scaling properties of velocity and temperature spectra above the surface friction layer in a convective atmospheric boundary layer. *Nonlinear Processes Geophys.,* **14,** 257–271, doi:10.5194/npg-14-257-2007.

Neggers, R., B. Stevens, and J. D. Neelin, 2006: A simple equilibrium model for shallow-cumulus-topped mixed layers. *Theor. Comput. Fluid Dyn.,* **20,** 305–322, doi:10.1007/s00162-006-0030-1.

Rennó, N. O., and Coauthors, 2013: CHASER: An innovative satellite mission concept to measure the effects of aerosols on clouds and climate. *Bull. Amer. Meteor. Soc.,* **94,** 685–694, doi:10.1175/BAMS-D-11-00239.1.

Reutter, P., and Coauthors, 2009: Aerosol- and updraft-limited regimes of cloud droplet formation: Influence of particle number, size and hygroscopicity on the activation of cloud condensation nuclei (CCN). *Atmos. Chem. Phys.,* **9,** 7067–7080, doi:10.5194/acp-9-7067-2009.

Rosenfeld, D., E. Williams, M. Andreae, E. Freud, U. Pöschl, and N. Rennó, 2012: The scientific basis for a satellite mission to retrieve CCN concentrations and their impacts on convective clouds. *Atmos. Meas. Tech.,* **5,** 2039–2055, doi:10.5194/amt-5-2039-2012.

——, B. Fischman, Y. Zheng, T. Goren, and D. Giguzin, 2014a: Combined satellite and radar retrievals of drop concentration and CCN at convective cloud base. *Geophys. Res. Lett.,* **41,** 3259–3265, doi:10.1002/2014GL059453.

——, G. Liu, X. Yu, Y. Zhu, J. Dai, X. Xu, and Z. Yue, 2014b: High-resolution (375 m) cloud microstructure as seen from the NPP/VIIRS satellite imager. *Atmos. Chem. Phys.,* **14,** 2479–2496, doi:10.5194/acp-14-2479-2014.

Saïd, F., G. Canut, P. Durand, F. Lohou, and M. Lothon, 2010: Seasonal evolution of boundary-layer turbulence measured by aircraft during the AMMA 2006 Special Observation Period. *Quart. J. Roy. Meteor. Soc.,* **136,** 47–65, doi:10.1002/qj.475.

Schmidt, H., and U. Schumann, 1989: Coherent structure of the convective boundary layer derived from large-eddy simulations. *J. Fluid Mech.,* **200,** 511–562, doi:10.1017/S0022112089000753.

Schumann, U., 1988: Minimum friction velocity and heat transfer in the rough surface layer of a convective boundary layer. *Bound.-Layer Meteor.,* **44,** 311–326, doi:10.1007/BF00123019.

Smedman, A.-S., U. Högström, J. C. R. Hunt, and E. Sahlée, 2007: Heat/mass transfer in the slightly unstable atmospheric surface layer. *Quart. J. Roy. Meteor. Soc.,* **133,** 37–51, doi:10.1002/qj.7.

Stull, R. B., 1985: A fair-weather cumulus cloud classification scheme for mixed-layer studies. *J. Climate Appl. Meteor.,* **24,** 49–56, doi:10.1175/1520-0450(1985)024<0049:AFWCCC>2.0.CO;2.

——, 1994: A convective transport theory for surface fluxes. *J. Atmos. Sci.,* **51,** 3–22, doi:10.1175/1520-0469(1994)051<0003:ACTTFS>2.0.CO;2.

Taylor, G. I., 1916: Conditions at the surface of a hot body exposed to the wind. Rep. Memo. of the British Advisory Committee for Aeronautics 272, Vol. 2, 423–429.

Tucker, S. C., C. J. Senff, A. M. Weickmann, W. A. Brewer, R. M. Banta, S. P. Sandberg, D. C. Law, and R. M. Hardesty, 2009: Doppler lidar estimation of mixing height using turbulence, shear, and aerosol profiles. *J. Atmos. Oceanic Technol.,* **26,** 673–688, doi:10.1175/2008JTECHA1157.1.

Twomey, S., 1959: The nuclei of natural cloud formation part II: The supersaturation in natural clouds and the variation of cloud droplet concentration. *Geofis. Pura Appl.,* **43,** 243–249, doi:10.1007/BF01993560.

Young, G. S., 1988a: Turbulence structure of the convective boundary layer. Part I: Variability of normalized turbulence statistics. *J. Atmos. Sci.,* **45,** 719–726, doi:10.1175/1520-0469(1988)045,0719:TSOTCB.2.0.CO;2.

——, 1988b: Turbulence structure of the convective boundary layer. Part II: Phoenix 78 aircraft observations of thermals and their environment. *J. Atmos. Sci.,* **45,** 727–735, doi:10.1175/1520-0469(1988)045,0727:TSOTCB.2.0.CO;2.

Zhu, Y., D. Rosenfeld, X. Yu, G. Liu, J. Dai, and X. Xu, 2014: Satellite retrieval of convective cloud base temperature based on the NPP/VIIRS Imager. *Geophys. Res. Lett.,* **41,** 1308–1313, doi:10.1002/2013GL058970.